Sensitivity analysis of unsteady RANS flows

Gammacurta, E.; Etienne, S.; Pelletier, D.; Ilinca, Florin

19th AIAA Computational Fluid Dynamics Conference [Proceedings], pp. 1-23, 2009-06

Sensitivity Analysis of Unsteady RANS Flows

E. Gammacurta,*S. Etienne,†

D. Pelletier‡

Ecole Polytechnique de Montréal, C.P. 6079, succ. Centre-ville, Montréal, Québec, H3C 3A7, Canada

F. Ilinca §

National Research Council of Canada, 75 de Mortagne, Boucherville, Québec, J4B 6Y4, Canada

In this paper, we presents a continuous sensitivity equation method (SEM) for Unsteady Reynolds-Averaged Navier-Stokes (URANS) simulations with an adaptative Finite Element Method. The development is performed for value parameters that do not affect the geometry of the computational domain. We use the standard $k-\epsilon$ model of turbulence with wall functions and some of its usual variants such as Kato-Launder modification and RNG. The logarithmic form of transport equations for k and ϵ are used. An adaptative remeshing algorithm is developed for time integration of the URANS equations. Formulation and implementation are first verified on a problem with a closed form solution : the decay grid turbulence. This is followed by applications to transient flow reaching a steady state for a backward facing step and vortex shedding behind a cylinder. Flow and sensitivity analyses are performed. Several uses of sensitivity information are demonstrated : identification of key parameters controlling the flow, assessing the influence of closure coefficients, and nearby solutions.

I. Introduction

Since the introduction of two equation turbulence models in CFD, the number of applications dealing with turbulent flows has considerably increased. Indeed, two equation models have shown to be a powerful tool to solve complex turbulent flows because they provide good predictions at reasonable cost (see R.H Nichols,[1] N.E Suhs *et al.*,[2] T. Schonfeld*et al.*[3]] . The use of wall functions has enjoyed a renewed interest in certain applications (see B. Mohammadi and G.Puigt[4]). With the constant progress of computer power, unsteady simulations of turbulent flows become a common occurrence. Finally, unstructured mesh adaptation has proved to be very efficient for steady computations as it allows to capture the behavior of small scale features of the physical phenomena. Furthermore, mesh adaptation allows to significantly reduce computational cost and control the accuracy of numerical solution (F. Hecht and B. Mohammadi[5]). Applications of adaptative grid to steady state flow problems abound in the literature. However, applications to unsteady flows are much less common and mostly deal with compressible inviscid flows (see R. Lohner and J.D. Baum,[6] R.D. Rausch *et al.*[7]). There is a paucity of papers on adaptative methods of unsteady turbulent incompressible flows. This is one of the aspects treated in this paper.

Furthermore, a continuous sensitivity equation method is used to provide additional capabilities to the URANS formulation and $k-\epsilon$ turbulence model such as the ability to identify of key parameters controlling

*Graduate student, Department de Génie Mécanique
†Research Fellow, Department de Génie Mécanique
‡Canada Research Chair, Department de Génie Mécanique, Associate Fellow AIAA
§Research officer, Industrial Materials Institute

the flow response, the ability to cascade uncertainties on the input parameters through the CFD code to obtain uncertainty estimates of the flow response, and a capability for fast estimation of nearby flows. Sensitivities are defined as the derivative of the flow field with respect to parameters of interest to the system. These can be physical properties of the fluid, boundary conditions or closure coefficients in the turbulence model. These parameters fall in the category of so-called value parameters which do not affect the geometry of the computational domain. Shape parameters are beyond the scope of this paper due to the special computational challenges they present.

The SEM for steady turbulent flow using the $k-\epsilon$ turbulence model was demonstrated by Turgeon *et al.*[8] More details about the general formulation of SEM and its implementation in an adaptative finite element solver are given in Turgeon *et al.*[9]

We cover a variety of flows; some present an initial transient before reaching a steady state (backward facing step), or square cylinder close to the ground. Others involve vortex shedding (circular cylinder). The latter require meshes that are able to adapt to the motion of convected structures like vortices.

The article is organized as follow. The first section introduces the URANS equations and the $k-\epsilon$ turbulence model. Details are given about logarithmic form of turbulence equations, wall functions and boundary conditions implementations. The sensitivity equations and their boundary conditions for value parameters are then described. Sensitivities of wall boundary conditions are also presented. A brief description of the Finite Element Method is given, and the solution algorithm is clearly illustrated. This second part ends with a paragraph devoted to adaptative methodology for unstructured mesh. In the third section, we present some selected cases :

- A closed form solution, the decay of grid turbulence, for code verification in the sense of Roache,[10]
- Flow over a backward facing step at a Reynolds number of 47625 that reaches a steady state,
- An unsteady vortex shedding simulation behind a circular cylinder

Finally, the paper ends with conclusions.

II. Flow Equations

A. Unsteady Reynolds-averaged Navier-Stokes equations

The flow regime of interest is modeled by the incompressible unsteady RANS equations :

$$\nabla \cdot \mathbf{u} = 0 \tag{1}$$

$$\rho\left(\frac{\partial \mathbf{u}}{\partial t} + \mathbf{u}\cdot\nabla\mathbf{u}\right) = -\nabla p + \nabla\cdot\left[(\mu+\mu_t)\left(\nabla\mathbf{u} + (\nabla\mathbf{u})^T\right)\right] + \mathbf{f} \tag{2}$$

where ρ is the fluid density, $\mathbf{u}$ the fluid velocity, p the fluid pressure, $\mathbf{f}$ a body force, μ and μ_t are respectively the viscosity and the eddy viscosity which is computed using the $k-\epsilon$ model of turbulence.

B. The standard $k-\epsilon$ model of turbulence

The eddy viscosity is expressed in terms of two turbulence variables k and ϵ, respectively the turbulence kinetic energy and its rate of dissipation. The eddy viscosity is given by :

$$\mu_t = \rho C_\mu \frac{k^2}{\epsilon} \tag{3}$$

The mathematical system is closed by using the standard $k-\epsilon$ model of turbulence (Launder and Spalding[11]). The transport equation for the turbulence kinetic energy is written :

$$\rho\left(\frac{\partial k}{\partial t} + \mathbf{u}\cdot\nabla k\right) = \nabla\cdot\left[\left(\mu + \frac{\mu_t}{\sigma_k}\right)\nabla k\right] + \mu_t P - \rho\epsilon \tag{4}$$

and for its rate of dissipation

$$\rho\left(\frac{\partial \epsilon}{\partial t}+\mathbf{u}\cdot\nabla\epsilon\right)=\nabla\cdot\left[\left(\mu+\frac{\mu_t}{\sigma_\epsilon}\right)\nabla\epsilon\right]+C_1\frac{\epsilon}{k}\mu_t P-C_2\rho\frac{\epsilon^2}{k} \tag{5}$$

where P, the production of turbulence is defined as

$$P=\nabla\mathbf{u}:\left(\nabla\mathbf{u}+\nabla\mathbf{u}^{\mathbf{T}}\right) \tag{6}$$

The constants C_μ, C_1, C_2, σ_k and σ_ϵ take the standard values recommended by Launder and Spalding[11] :

$$C_\mu=0.09, \qquad C_1=1.44, \qquad C_2=1.92, \qquad \sigma_k=1.0, \qquad \sigma_\epsilon=1.3$$

C. Logarithmic form of the turbulence equations

In some cases, the turbulence equations may cause numerical difficulties. For example, the eddy viscosity may become negative if one of turbulence variables becomes negative. This can cause a dramatic breakdown of the solver. Also, several source terms contain division by k or ϵ. Negative or very small values of the denominator may lead to improper signs or overly large values for the eddy viscosity or source terms. Therefore, maintaining turbulence variables positive throughout the domain and the course of iterations, will resulting in algorithm enhanced robustness. In order to preserve positivity of the turbulence variables, F. Ilinca,[12] F.Ilinca and D. Pelletier[13] suggested to use the logarithms of k and ϵ as dependent variables :

$$\mathcal{K}=ln(k), \qquad \mathcal{E}=ln(\epsilon)$$

Solving for $\mathcal{K}$ and $\mathcal{E}$ guarantees that k and ϵ will remain positive throughout the computations. Thus, the eddy viscosity will always remain positive. Moreover, turbulence quantities often present very steep fronts which are difficult to solve accurately. The fields of the logarithmic variables $\mathcal{K}$ and $\mathcal{E}$ present smoother variations than those of k and ϵ because the logarithm varies more smoothly than its argument. Hence, very accurate solutions are obtained with logarithmic variables. The logarithmic form of the transport equation for are:

$$\rho\left(\frac{\partial \mathcal{K}}{\partial t}+\mathbf{u}\cdot\nabla\mathcal{K}\right)=\nabla\cdot\left[\left(\mu+\frac{\mu_t}{\sigma_k}\right)\nabla\mathcal{K}\right]+\mu_t e^{-\mathcal{K}}P-\rho e^{\mathcal{E}-\mathcal{K}} \tag{7}$$

and

$$\rho\left(\frac{\partial \mathcal{E}}{\partial t}+\mathbf{u}\cdot\nabla\mathcal{E}\right)=\nabla\cdot\left[\left(\mu+\frac{\mu_t}{\sigma_\epsilon}\right)\nabla\mathcal{E}\right]+C_1\mu_t e^{-\mathcal{K}}P-C_2\rho e^{\mathcal{E}-\mathcal{K}} \tag{8}$$

The eddy viscosity is now computed in the following manner :

$$\mu_t=\rho C_\mu e^{2\mathcal{K}-\mathcal{E}} \tag{9}$$

It is important to note that the equations for logarithmic variables are equivalent to the original equations of $k-\epsilon$ (see equations (4) and (5)). Thus the turbulence model remains unchanged. The only modification is that the computational variables are now the logarithms of the turbulence quantities. Finally, the use of logarithmic form has removed the potentially troublesome divisions by k and ϵ and a number of other worrisome divisions, thus improving the convergence of the solver. The only drawback of this method is the appearance of exponentials in the right-hand side of the turbulence equations. However, since k and ϵ take on small values, the exponential is very flat so that the non-linearities are mild.

D. Common variants of the $k-\epsilon$ model

Among the common variants of the $k-\epsilon$ model, the Kato-Launder[14] modification (KL) is probably one of the most famous. This modification reduces the tendency of many two-equation models to over-predict the turbulent production near stagnation points and in small regions with strong acceleration and deceleration. The modification was originally developed for simulations of vortex-shedding behind a square cylinder. It consists in modifying the production of turbulence P to be:

$$P = \left[\nabla \mathbf{u} : \left(\nabla \mathbf{u} + \nabla \mathbf{u}^{\mathbf{T}}\right)\right]^{0.5} * \left[\nabla \mathbf{u} : \left(\nabla \mathbf{u}^{\mathbf{T}} - \nabla \mathbf{u}\right)\right]^{0.5} \tag{10}$$

The second modification was proposed by B.A. Younis and V.P. Przulj[15] (YP) and consists in modifying the turbulent production term in the transport equation of $\mathcal{E}$. The constant C_1 is replaced as follows :

$$C_1^* = C_1 \left(1 + C_t e^{\mathcal{K}-\mathcal{E}} \frac{1}{Q/e^{\mathcal{K}}+1} \left|\frac{\partial\left(Q+e^{\mathcal{K}}\right)}{\partial t}\right|\right) \tag{11}$$

where Q is the mean-flow kinetic energy and C_t a new constant equal to 0.38. This modification accounts for the interactions between the large-scale organized flow structures of the mean flow and the random, small-scale high-frequency motions that characterize turbulence.

Finally, the last variant of used here is the Personalization Group (RNG) model of Yakhot *et al.*[16] The RNG uses a modified form of the transport equation for $\mathcal{E}$ to account for the different scales of motion through a modified production term:

$$C_1^* = C_1 - \frac{C_\mu \eta^3 \left(1-\eta/\eta_0\right)}{1+\beta\eta^3} \tag{12}$$

where $\eta = \sqrt{P} * e^{(\mathcal{K}-\mathcal{E})}$, η_0 and β are two new constants. Finally, the values of the five closure coefficients of the $k-\epsilon$ model are adjusted to

$$\begin{array}{lll} C_\mu = 0.0845, & C_1 = 1.42, & C_2 = 1.68, \\ \sigma_k = 0.72, & \sigma_\epsilon = 0.72, & \eta_0 = 4.38, \\ \beta = 0.012 & & \end{array}$$

E. Boundary conditions

The flow in the domain Ω is modeled by the URANS equations subject to boundary conditions. Typical boundary conditions take the following forms :

$$\mathbf{u} = \mathbf{u_{bc}} \qquad \text{on} \qquad \mathbf{\Gamma_d} \tag{13}$$

for Dirichlet boundary conditions, and

$$-p + \widehat{\mathbf{n}} \cdot \tau(\mathbf{u}) \cdot \widehat{\mathbf{n}} = 0 \qquad \text{and} \qquad \mathbf{u} \cdot \widehat{\mathbf{t}} = 0 \qquad \text{on} \qquad \mathbf{\Gamma_n} \tag{14}$$

for outflow condition (Neumann boundary condition), or

$$\mathbf{u} \cdot \widehat{\mathbf{n}} = 0 \qquad \text{and} \qquad \widehat{\mathbf{t}} \cdot \tau(\mathbf{u}) \cdot \widehat{\mathbf{n}} = 0 \qquad \text{on } \mathbf{\Gamma_s} \tag{15}$$

to model symmetry. The stress tensor $\tau(u)$ is defined as

$$\tau(\mathbf{u}) = (\mu + \mu_t)\left(\nabla \mathbf{u} + (\nabla \mathbf{u})^{\mathbf{T}}\right) \tag{16}$$

Similarly, the boundary conditions for k and ϵ are

$$\mathcal{K} = ln(k_{bc}) \quad \text{on} \quad \Gamma_{dk} \tag{17}$$

$$\mathcal{E} = ln(\epsilon_{bc}) \quad \text{on} \quad \Gamma_{d\epsilon} \tag{18}$$

for Dirichlet boundary conditions, and

$$\left[\left(\mu + \frac{\mu_t}{\sigma_k}\right)\nabla\mathcal{K}\right]\cdot\hat{\mathbf{n}} = 0 \quad \text{on} \quad \Gamma_{nk} \tag{19}$$

$$\left[\left(\mu + \frac{\mu_t}{\sigma_\epsilon}\right)\nabla\mathcal{E}\right]\cdot\hat{\mathbf{n}} = 0 \quad \text{on} \quad \Gamma_{n\epsilon} \tag{20}$$

for Neumann boundary condition.

F. Wall boundary conditions

The standard $k-\epsilon$ turbulence model is not valid near solid walls. Wall functions are used in order to describe the solution near the wall. A two-velocity scale wall functions described in J.P Chabard[17] and L. Ignat *et al.*[18] The universal velocity profile is given by :

$$u^+ = \begin{cases} y^+ & \text{for } y^+ < y_c^+ \\ \frac{1}{\kappa} ln\,(Ey^+) & \text{for } y^+ \geq y_c^+ \end{cases} \tag{21}$$

where κ is the Karman constant and E a roughness parameter. For smooth walls, $\kappa = 0.42$ and $E = 9.0$ are appropriate values. The definition of u^+ highlight the existence of two distinct regions. The first one for $y^+ < y_c^+$ is called laminar sub-layer, the second one for $y^+ \geq y_c^+$ is called logarithmic layer. The transition point y_c^+ is obtained from the intersection of the two curves $y_c^+ \approx 11$. The dimensionless wall distance y^+ and tangential velocity u^+ are given by :

$$y^+ = \frac{\rho y u_k}{\mu} \tag{22}$$

$$u^+ = \frac{u_t}{u_{**}} \tag{23}$$

where u_t is the tangential velocity and y is the normal distance to the wall. There are two velocity scales :

- $u_{**} = \sqrt{\tau_w/\rho}$, friction velocity (with τ_w the wall shear stress)
- u_k a velocity scale based on the turbulence kinetic energy and defined as

$$u_k = C_\mu^{1/4} exp\,(\mathcal{K}_w/2) \tag{24}$$

where $\mathcal{K}_w$ is $\mathcal{K}$ taken at the boundary of the computational domain. The corresponding boundary conditions for $\mathcal{K}$, $\mathcal{E}$ and the momentum equations at a distance $y = d$ from the wall are :

$$\tau_w = \rho u_k u_{**} = \frac{\rho u_k}{\frac{1}{\kappa} ln\left(E\frac{\rho d u_k}{\mu}\right)} u_t \tag{25}$$

$$\mathbf{u}\cdot\hat{\mathbf{n}} = \mathbf{0} \tag{26}$$

$$\frac{\partial k}{\partial n} = 0 \quad \text{or} \quad \left(\mu + \frac{\mu_t}{\sigma_k}\right)\nabla\mathcal{K}\cdot\hat{\mathbf{n}} = \mathbf{0} \tag{27}$$

$$\mathcal{E} = ln\left(\frac{u_k^3}{\kappa d}\right) \tag{28}$$

where $\hat{\mathbf{n}}$ is the outward normal unit vector. Note that the substitution of equations (21-23) provides a relationship between the wall shear stress τ_w and the velocity u_t, this is called mixed or Robin boundary condition.

III. Sensitivity Equations

A. Sensitivity equations for the Unsteady Reynolds-averaged Navier-Stokes equations

The continuous sensitivity equations are derived formally by implicit differentiation of the flow equations (1) and (2) with respect to design parameter a. Thus, we treat the variable $\mathbf{u}$ as a function of space and as a function of the design parameter a. This dependence is denoted as $\mathbf{u}(\mathbf{x};a)$. We define the flow sensitivities as the partial derivatives $\mathbf{S}_u = \frac{\partial \mathbf{u}}{\partial a}$ and $S_p = \frac{\partial \mathbf{p}}{\partial a}$ and the total derivatives of the fluid properties and other flow parameters by ('). Following a general approach, we obtain :

$$\nabla \cdot \mathbf{S}_u = 0 \tag{29}$$

$$\rho' \left(\frac{\partial \mathbf{u}}{\partial t} + \mathbf{u} \cdot \nabla \mathbf{u} \right) + \rho \left(\frac{\partial \mathbf{S}_u}{\partial t} + \mathbf{S}_u \cdot \nabla \mathbf{u} + \mathbf{u} \cdot \nabla \mathbf{S}_u \right) = \tag{30}$$

$$-\nabla S_p + \nabla \cdot \left[(\mu' + \mu_t') \left(\nabla \mathbf{u} + (\nabla \mathbf{u})^T \right) + (\mu + \mu_t) \left(\nabla \mathbf{S}_u + (\nabla \mathbf{S}_u)^T \right) \right] + \mathbf{f}'$$

B. Turbulence sensitivity equations

Differentiation of the turbulence transport equations (4) and (5) with respect to parameter a yields the continuous sensitivity equations for $S_\mathcal{K}$ and $S_\mathcal{K}$. Following the general approach, these equations take the form :

$$\rho' \left(\frac{\partial \mathcal{K}}{\partial t} + \mathbf{u} \cdot \nabla \mathcal{K} \right) + \rho \left(\frac{\partial S_\mathcal{K}}{\partial t} + \mathbf{S}_u \cdot \nabla \mathcal{K} + \mathbf{u} \cdot \nabla S_\mathcal{K} \right) = \tag{31}$$

$$\begin{aligned}
&\nabla \cdot \left[\left(\mu' + \frac{\mu_t'}{\sigma_k} - \frac{\mu_t \sigma_k'}{\sigma_k^2} \right) \nabla \mathcal{K} + \left(\mu + \frac{\mu_t}{\sigma_k} \right) \nabla S_\mathcal{K} \right] \\
&+ \left(\mu' + \frac{\mu_t'}{\sigma_k} - \frac{\mu_t \sigma_k'}{\sigma_k^2} \right) \nabla \mathcal{K} \cdot \nabla \mathcal{K} + 2 \left(\mu + \frac{\mu_t}{\sigma_k} \right) \nabla \mathcal{K} \cdot \nabla S_\mathcal{K} \\
&+ (\mu_t' P + \mu_t P' - \mu_t P S_\mathcal{K}) \, e^{-\mathcal{K}} - \rho \left(2 \frac{\rho'}{\rho} + \frac{C_\mu'}{C_\mu} + S_\mathcal{K} - \frac{\mu_t'}{\mu_t} \right) e^{\mathcal{E}-\mathcal{K}}
\end{aligned}$$

and

$$\rho' \left(\frac{\partial \mathcal{E}}{\partial t} + \mathbf{u} \cdot \nabla \mathcal{E} \right) + \rho \left(\frac{\partial S_\mathcal{E}}{\partial t} + \mathbf{S}_u \cdot \nabla \mathcal{E} + \mathbf{u} \cdot \nabla S_\mathcal{E} \right) = \tag{32}$$

$$\begin{aligned}
&\nabla \cdot \left[\left(\mu' + \frac{\mu_t'}{\sigma_\epsilon} - \frac{\mu_t \sigma_\epsilon'}{\sigma_\epsilon^2} \right) \nabla \mathcal{E} + \left(\mu + \frac{\mu_t}{\sigma_\epsilon} \right) \nabla S_\mathcal{E} \right] \\
&+ \left(\mu' + \frac{\mu_t'}{\sigma_\epsilon} - \frac{\mu_t \sigma_\epsilon'}{\sigma_\epsilon^2} \right) \nabla \mathcal{E} \cdot \nabla \mathcal{E} + 2 \left(\mu + \frac{\mu_t}{\sigma_\epsilon} \right) \nabla \mathcal{E} \cdot \nabla S_\mathcal{E} \\
&+ \rho C_1 C_\mu P \left(\frac{\rho'}{\rho} + \frac{C_1'}{C_1} + \frac{C_\mu'}{C\mu} + S_\mathcal{K} - S_\mathcal{E} + \frac{P'}{P} \right) e^{\mathcal{K}-\mathcal{E}} \\
&- \rho C_2 \left(\frac{\rho'}{\rho} + \frac{C_2'}{C_2} + S_\mathcal{E} - S_\mathcal{K} \right) e^{\mathcal{E}-\mathcal{K}}
\end{aligned}$$

where the sensitivity of the production term is

$$P' = 2 \nabla \mathbf{S}_u : \left(\nabla \mathbf{u} + \nabla \mathbf{u}^\mathbf{T} \right) \tag{33}$$

and the sensitivity of the eddy viscosity is

$$\begin{aligned}
\mu_t' &= \left(\rho' C_\mu + \rho C_\mu' \right) e^{2\mathcal{K}-\mathcal{E}} + \rho C_m u \left(2 S_\mathcal{K} - S_\mathcal{E} \right) e^{2\mathcal{K}-\mathcal{E}} \\
&= \mu_t \left(\frac{\rho'}{\rho} + \frac{C_\mu'}{C_\mu} + 2 S_\mathcal{K} - S_\mathcal{E} \right)
\end{aligned} \tag{34}$$

The sensitivities of the turbulence logarithmic variables are used for numerical computations. However, if the analysis requires the sensitivities of k and ϵ ($S_\mathcal{K}$ and $S_\mathcal{E}$), the following transformation may be used :

$$\begin{aligned} S_k &= kS_\mathcal{K} \\ S_\epsilon &= \epsilon S_\mathcal{E} \end{aligned}$$

C. Sensitivity boundary conditions

The sensitivity boundary conditions are also derived by implicit differentiation of the flow boundary conditions (13-20). We assume that the boundary is parameter independent. The more general case of shape parameters is treated by Turgeon *et al.*[19] where a unified approach for shape and value parameters was developed for laminar flows. However, the computation of sensitivities for wall function applied to a parameter dependent boundary (shape sensitivity) requires the evaluation of the second derivatives of the flow along the boundary of the computational domain, a very challenging task. Therefore, we focus our attention on value parameters. For a value parameter, the Dirichlet boundary condition for the sensitivities corresponding to (13) is thus :

$$\mathbf{S}_u = \mathbf{u'_{bc}} \qquad \text{on} \qquad \mathbf{\Gamma_d} \tag{35}$$

For the outflow conditions (14), we get :

$$-S_p + \widehat{\mathbf{n}} \cdot \tau'(\mathbf{u}) \cdot \widehat{\mathbf{n}} = \mathbf{0} \qquad \text{and} \qquad \mathbf{S_u} \cdot \widehat{\mathbf{t}} = \mathbf{0} \qquad \text{on} \qquad \mathbf{\Gamma_n} \tag{36}$$

Similar manipulations are performed for the remaining boundary conditions.
It is important to note that, for all parameters, the continuous sensitivity equations (CSE) have the same structure and the same type of boundary conditions as the flow equations. This is important, since it results in the same structure for the variational form of the flow and sensitivity systems. Of course, this implies that the sensitivity equations solver has the same code organization as the flow solver.

D. Sensitivity of wall boundary conditions

Wall functions for sensitivity equations are obtained by implicit differentiation of wall functions of the flow equations. As the normal and tangent vectors have zero derivative with respect to a, differentiation is simplified for value parameters. Differentiation of the no-penetration condition (26) leads to

$$\mathbf{S_u} \cdot \widehat{\mathbf{n}} = 0 \tag{37}$$

whereas the sensitivity of the shear stress is given by differentiation of (25)

$$\tau'_w = \rho' u_k u_{**} + \rho u'_k u_{**} + \rho u_k u'_{**} \tag{38}$$

The sensitivities of u'_{**} and u'_k appearing in this expression are obtained by differentiation of equations (23) and (24)

$$u'_{**} = \frac{u'_t}{u^+} - \frac{u_t u^{+\prime}}{u^{+2}} \tag{39}$$

$$u'_k = u_k \left(\frac{1}{4} \frac{C'_\mu}{C_\mu} + \frac{1}{2} S_\mathcal{K} \right) \tag{40}$$

where, from equation (21)

$$u^{+\prime} = \begin{cases} y^{+\prime} & \text{for } y^+ < y_c^+ \\ \frac{1}{\kappa} \left(-u^+ \kappa' + \frac{E'}{E} + \frac{y^{+\prime}}{y^+} \right) & \text{for } y^+ \geq y_c^+ \end{cases} \tag{41}$$

and from equation (22)

$$y^{+\prime} = y^{+}\left(\frac{\rho'}{\rho} + \frac{d'}{d} + \frac{u'_k}{u_k} - \frac{\mu'}{\mu}\right). \tag{42}$$

Finally, for the tangential component of velocity

$$u_t = ut_x + vt_y \tag{43}$$

we get

$$u'_t = S_u t_x + S_v t_y \tag{44}$$

Here we have assumed that $t'_x = t'_y = 0$ because only value parameters are considered. Note that even if the computational boundary is fixed, the distance to the wall d may vary yet the computational domain remains unchanged. Thus, we simply consider d as a value parameter in the wall functions.
From equation (27) we deduce the following boundary condition for $S_\mathcal{K}$

$$\frac{\partial S_\mathcal{K}}{\partial n} = 0 \tag{45}$$

which can be written in a form more suitable for the natural boundary conditions of the finite element formulation :

$$\left[\left(\mu' + \frac{\mu'_t}{\sigma_k} - \frac{\mu_t \sigma'_k}{\sigma_k^2}\right)\nabla\mathcal{K} + \left(\mu + \frac{\mu_t}{\sigma_k}\right)\nabla S_\mathcal{K}\right]\cdot\widehat{\mathbf{n}} = 0 \tag{46}$$

Finally, the boundary condition for $S_\mathcal{E}$ is :

$$S_\mathcal{E} = 3\frac{u'_k}{u_k} - \frac{\kappa'}{\kappa} - \frac{d'}{d} \tag{47}$$

The above expression for the sensitivity boundary conditions are derived once and for all. The specification of sensitivities of the coefficients appearing in the boundary conditions (ρ', μ', d', κ' and e') define the appropriate boundary conditions for a given parameter a for the sensitivity equations.

IV. Implementation

A. Finite Element Solver

The URANS and continuous sensitivity equations are solved with the Galerkin finite element method (F. Ilinca *et al.*[20] and F. Ilinca and D. Pelletier[13]). The equations are first multiplied by a test function W and then integrated over the computational domain. The diffusion terms are integrated by parts using the divergence theorem. This introduces the so-called natural boundary conditions involving the normal component of the diffusion flux at the boundary. It also transfers some of the derivatives from the solution onto the test function. This approach is also applied to the turbulence equations. For highly convective flow some form of stabilization might be required such as SUPG. This usually result in smoother flows and better results, in terms on adaptative mesh quality.

The velocity and pressure are discretized using the Taylor-Hood triangular element which use a quadratic polynomial for velocity and piecewise linear continuous approximation for the pressure. The logarithmic variables are also discretized with piecewise quadratic polynomial approximation. The equations are linearized by Newton's method. The resulting system of linear algebraic equations is solved using a Parallel Sparse Direct Solver, PARDISO (O. Schenk and K. Gärtner[21,22]).

B. Solution algorithm

The numerical solution algorithm proceeds in the following partly segregated manner. At each time step, the momentum and continuity equations are solved for a given field of μ_t. The $\mathcal{K}$ and $\mathcal{E}$ equations are then solved

sequentially. Sub-iterations on the turbulence equations accelerate the overall convergence of the process. This loop is repeated until convergence is achieved. This process is repeated for each time step. The solution algorithm is illustrated in Fig 1.
Once the flow solution is obtained, at a given time-step CSE systems are solved successively following the same algorithm. Flow and sensitivity equations share the same time loop. Finally, note that the same mesh and finite elements are used for both the flow and its sensitivities.

C. Adaptative Methodology

The adaptative remeshing procedure used here is modeled on that proposed by J. Peraire[23] and is described in more detail by F. Ilinca,[12] D. Pelletier and F. Ilinca[24]]. The procedure refines the grid in regions of rapid variations for all dependent variables. Error estimates are obtained by a local least squares reconstruction of the solution derivatives (O. C Zienkiewicz and J. Z Zhu[25,26]). For the velocity field, the strain rate tensor is used for error estimation. An error estimate of the pressure solution is obtained by a local projection of the pressure field itself. Error estimates are also obtained for the turbulence variables by projecting the finite element derivatives of $\mathcal{K}$ and $\mathcal{E}$ into a continuous field. Finally, an error estimate for the eddy viscosity is also computed since slowly varying fields of $\mathcal{K}$ and $\mathcal{E}$ can result in rapid variation of the eddy viscosity. This is essential to the success of adaptation in turbulent flows since the eddy viscosity is the sole mechanism for diffusion of momentum and turbulence kinetic energy by turbulent fluctuations. See F. Ilinca *et al.*,[20,27] D. Pelletier and F. Ilinca[24]] for examples and some discussions of these issues. When sensitivities are computed, error estimates are obtained for all flow variables and all their sensitivities. The grid is thus adapted for both the flow and its sensitivities.

Once the error estimates are obtained for all dependent variables, a better mesh must be designed. In our approach, all variables are analyzed and contribute to the mesh adaptation process. For this, an error estimate is obtained separately for each dependent variable. The mesh characteristics (element size) are derived for each variable on a given element. The mesh is designed so as to result in a reduction of the error by a user-specified factor. The minimum element size predicted by each of the dependent variables is selected on each element. The process of solution, error estimation and remeshing is repeated until satisfactory accuracy is achieved. Details of this algorithm have been presented previously in Ilinca,[12] Turgeon[28] and F. Ilinca *et al.*[29]

If an adaptative mesh generation routine is used for the flow, then the CSE only need to be computed on the finest mesh. However, we choose to solve the CSE at each cycle of mesh adaptation and use error estimates of all the sensitivity variables in the mesh refinement scheme. This allows a better control of the sensitivity solution accuracy because a good adaptative mesh for the flow solution may not necessarily be a good mesh for the sensitivity solution (see J.Borggaard and D.Pelletier[30] and D.Pelletier *et al.*[31]).

The original adaptative algorithm was designed to achieve a preset level of accuracy for steady state problems. The adaptative strategy is set to reduce the global error by a constant factor at each cycle of grid adaptation. A satisfactory grid is usually obtained after a few adaptative cycles (less than ten). This works well for steady flows and for unsteady flows that reach a steady state after an initial transient phase. Here we focus on truly unsteady flows such as vortex shedding behind an obstacle (circular cylinder, square in ground proximity). These are characterized by the fact that flow structures are convected through the domain. To maintain good resolution and accuracy it becomes important that the mesh be able to adapt to the motion of the flow to accurately track flow features of interest.

Typically, an initial grid is designed and an initial solution is set to that of a fluid at rest or to a steady state flow solution. Time integration ia carried out for a few time steps, the solver switched to the error estimation and grid adaption, the procedure is configured to attempt to reduce the error ny a constant factor. A new mesh is generated, the solution interpolated quadratically from the current mesh to the new one. and the process is repeated until the grids has acquired an appropriate degree of refinement to resolve the flow feature adequately. From there on, the grid ia adapted approximately 10 to 12 times per period. setting the error reduction ration to one, generates a grid better adapted to the flow structure motion.

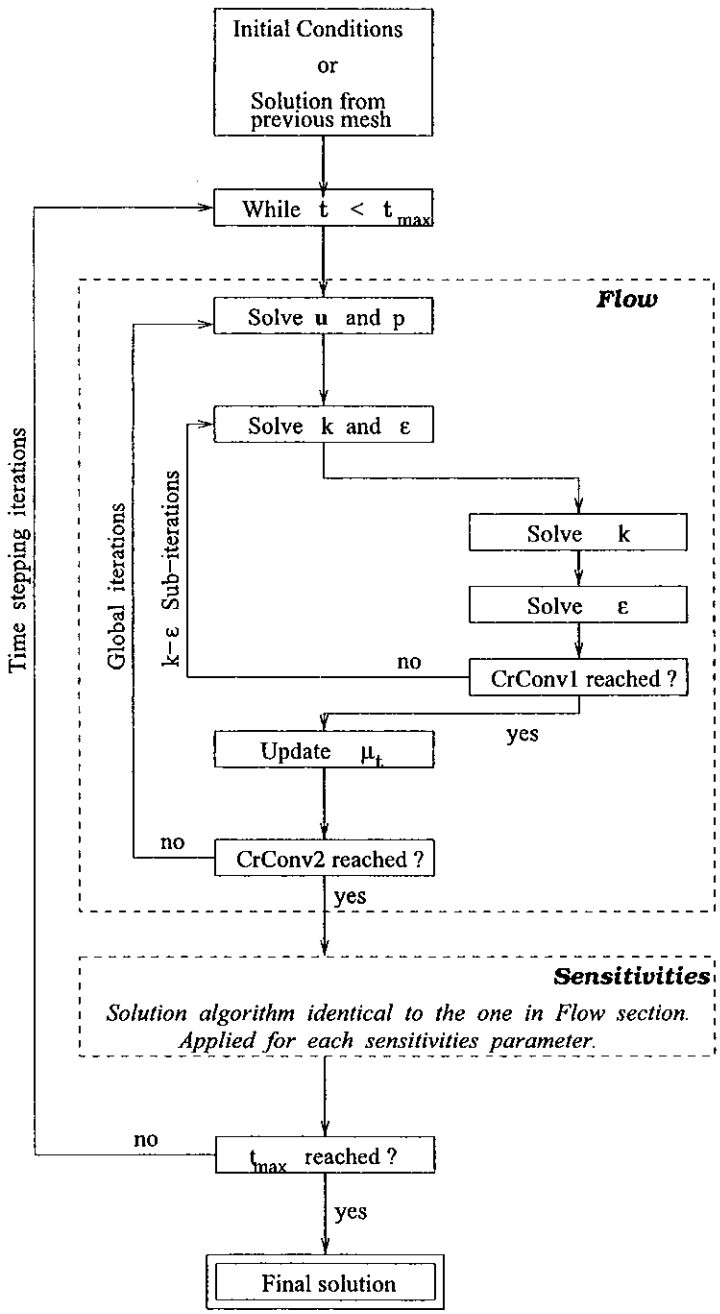

Figure 1. Solution algorithm

V. Numerical results

We present selected results for a few test cases :

- Decay of grid turbulence, a closed form solution to perform code verification,
- Impulsively started flow over a backward facing step reaching a steady state after an initial transient phase
- Vortex shedding behind a circular cylinder at a Reynolds number of 10000

A. Verification : the decay grid turbulence

Verification is essential before proceeding to applications (see Roache[10]). Verification is performed on problems possessing a closed form solution. Here, the problem considered is the decay of grid turbulence in a uniform flow, as presented by Ilinca *et al.*,[32] which has an analytical solution. μ and C_μ are set to extremely low values so that diffusion terms become negligible. The exact solution is given by :

$$\begin{aligned} u &= 1, \\ v &= 0, \\ p &= 0, \\ k &= \epsilon_0 \left(\frac{\epsilon_0}{k_0}\right)^{-\frac{C_2}{C_2-1}} \left[(C_2-1)\,x + \frac{k_0}{\epsilon_0}\right]^{-\frac{1}{C_2-1}}, \\ \epsilon &= \epsilon_0 \left(\frac{\epsilon_0}{k_0}\right)^{-\frac{C_2}{C_2-1}} \left[(C_2-1)\,x + \frac{k_0}{\epsilon_0}\right]^{-\frac{C_2}{C_2-1}} \end{aligned} \tag{48}$$

where k_0 and ϵ_0 are the turbulence kinetic energy and the turbulence dissipation at the inlet ($x = 0$). The computational domain extends from (0,0) to (1,0.2). Dirichlet boundary conditions are applied at the inlet, while zero Neumann conditions are applied everywhere else. For the unsteady simulation, a large time value is set. For the sensitivity computations, k_0, ϵ_0 and C_2 are the parameters of interest. The exact sensitivities are obtained by differentiation of the exact flow simulation.

Figures 2 and 3 show the distribution of $\mathcal{K}$, $\mathcal{E}$, $S_\mathcal{K}$ and $S_\mathcal{E}$ along the line $y = 0.1$. These results were obtained after three cycles of adaptation on a mesh containing 3463 nodes. As can be seen, the overlap is so nearly perfect that the numerical predictions are indistinguishable from the exact solutions. This confirms the accuracy of predictions and ability of the code to deliver the right solution to the equations for both the flow and its sensitivities.

B. Turbulent flow over a backward facing step

Our first application is the flow over a backward facing step studied experimentally by Kim (1978). The Reynolds number is $Re = 47625$ based on the step height L. More details will be found in E. Turgeon *et al.*[8] The computation domain is illustrated in Fig 4.

The boundary conditions are given in Table 1.

At time t_0, the flow is impulsively started from rest and will reach a steady state after a sufficiently long period of time. Figure 5 shows meshes with contours of U for three values of time. The initial grid at t_0 contains 41496 nodes and was obtained after 4 cycles of adaptation. Figure 5 (a) shows the grid obtained at time t_1 when the flow just reached the corner. The grid is refined near the corner because of the sharp gradient and curvature in the solution fields. It is important to note that refinement along the walls downstream

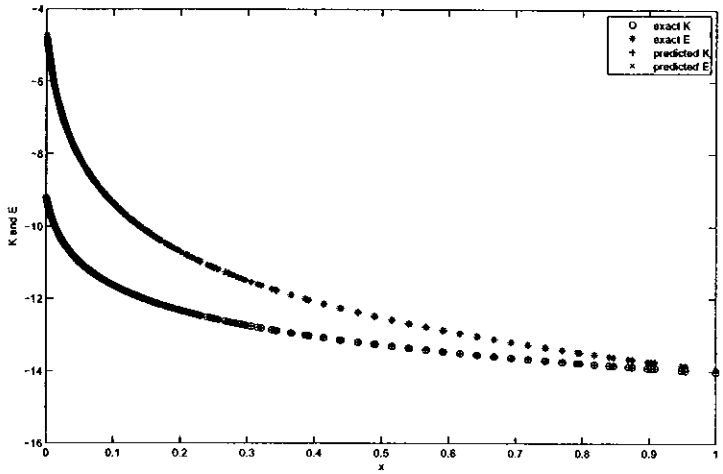

Figure 2. comparison between numerical and exact solutions for $\mathcal{K}$ and $\mathcal{E}$

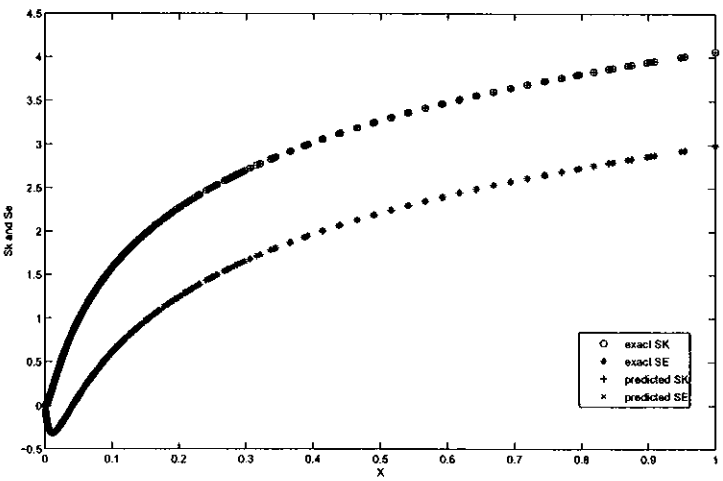

Figure 3. comparison between numerical and exact solutions for $S_{\mathcal{K}}$ and $S_{\mathcal{E}}$

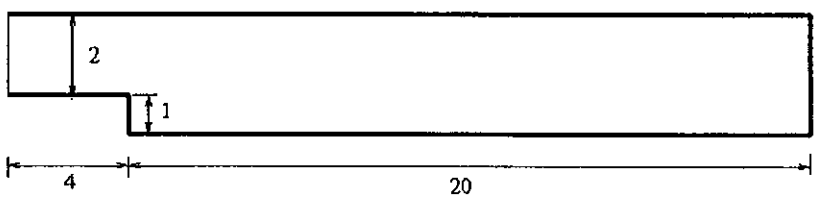

Figure 4. Computation domain

Inlet	outlet
$u = 1$	$-p + 2(\mu + \mu_t)\frac{\partial u}{\partial x} = 0$
$v = 0$	$v = 0$
$k = 0.005$	$\frac{\partial k}{\partial x} = 0$
$\epsilon = 0.01$	$\frac{\partial \epsilon}{\partial x} = 0$

Table 1. Boundary conditions for the inlet and outlet

from the corner is due to the initial mesh. At time t_2 the inflow profile has penetrated to three-quarters of the domain. As can be seen the mesh is adapted to the motion of the flow. On the top wall the boundary layer develops as one would expect. On the bottom wall, the grid evolution reflects the complex interaction between the recirculation zone and the boundary layer. At time t_f, a steady state is reached. The final mesh contains 78503 nodes and is clearly refined in the shear layer emanating from the step corner and the two boundary layers on the top and bottom walls. The final results are very similar to the results obtained by Turgeon *et al.*[8] with a steady state formulation.

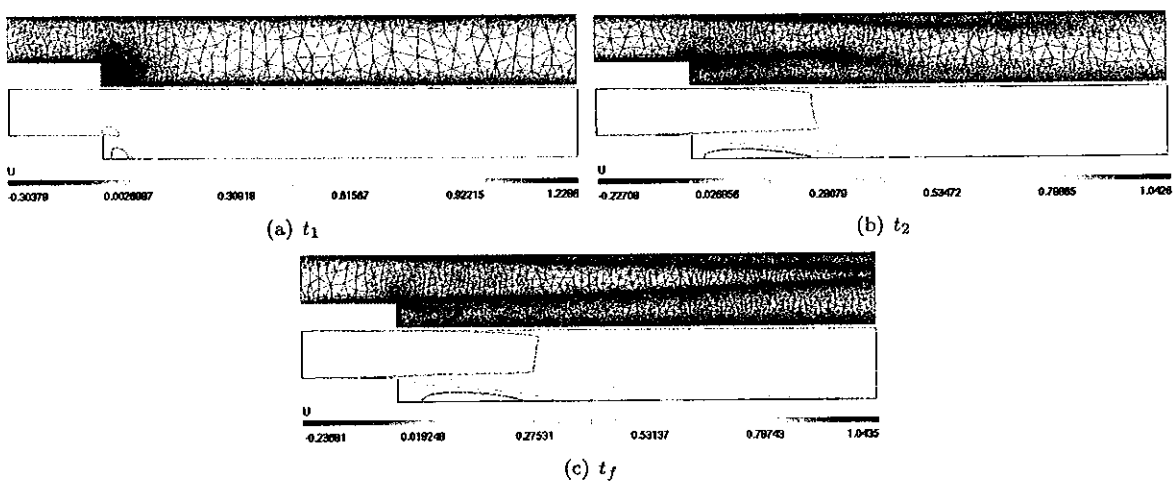

(a) t_1 (b) t_2

(c) t_f

Figure 5. Adaptative remeshing for the backward facing step at various time step

Seven parameters are considered for sensitivity analysis :

- $kinf$ and $einf$, turbulence variables inflow boundary values
- C_μ, C_1, C_2, σ_k and σ_ϵ. the five closure coefficients of the standard $k - \epsilon$ model,

First Figure 6 provides details about the sensitivities of u and the vorticity Ω of the sensitivities velocity with respect to parameter $kinf$. Note that an increase of k at the inlet will energize the boundary and shear layers. On the one hand Su_{kinf} is a measure of the influence of parameter $kinf$ on the flow fields. as can be seen, its effect is most pronounced along the top wall and in a narrow band emanating from the upstream corner. Notice that $kinf$ also has some influence in the vicinity of the recirculation zone on the bottom wall.

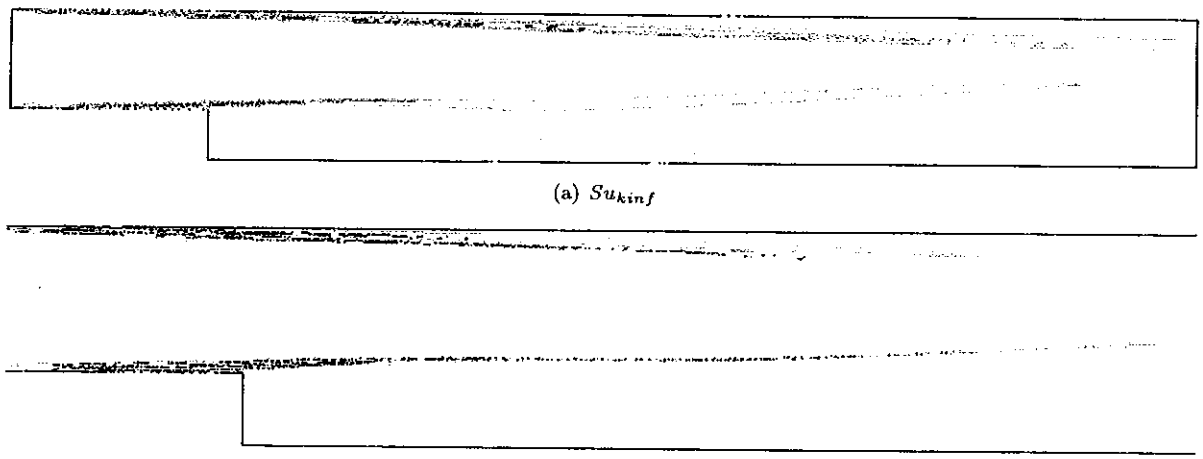

(a) Su_{kinf}

(b) $\Omega(Su_{kinf}, Sv_{kinf})$

Figure 6. Solution contour of Su_{kinf} and $\Omega(Su_{kinf}, Sv_{kinf})$ at t_f

On the other hand, $\Omega(Su_{kinf}, Sv_{kinf})$, the vorticity of the velocity sensitivity, indicates that an increase in $kinf$ results in a thickening of the boundary layers along the horizontal walls.

These observations are confirmed by Figures 7 and 8. Figure 7 presents the profile of streamwise velocity U extracted from the solution at the nominal values of all parameters and the Taylor series estimates of the profile for a 10% increase of each parameter taken individually. This corresponds to valuating the following expression

$$\mathbf{u}(x, y; a + \Delta a) = \mathbf{u}(x, y; a) + \frac{\partial \mathbf{u}}{\partial a} \Delta a \tag{49}$$

which provides a so-called fast estimate of a nearby flow corresponding to a 10 % increase in parameter a. In the above equation $Su_a = \frac{\partial \mathbf{u}}{\partial a}$. Δa is a variation of parameter a. Here we use $\Delta_a = 10\% a$

Figure 7 shows the profiles of u and the nearby solution with respect to the seven parameters. Note that C_μ and C_1 are the most influential parameters as far as the recirculation zone is concerned. An increase of C_μ significantly reduces the length of the recirculation zone. So do C_2, $kinf$ and σ_k to a lesser extent. On the other hand, σ_e is not an influential parameter at all. Finally, $einf$ and ,above all, C_1 increase the size of the recirculation zone and the strength of the recirculating flow.

Figure 8 shows the vorticity profile and its sensitivities with respect to $kinf$ and $einf$. The profiles are shown for two stations : $x/L = -0.5$, upstream of the step, and $x/L = 18$, almost at the end of the domain. For clarity reasons, only the effects of $kinf$ and $einf$ are shown. The influence of the other parameters C_1 and σ_k is similar to that of $einf$ but with a much smaller effects on the profiles of the vorticity of the velocity sensitivity. Increasing the value of these parameters increases and strengthen the vorticity in the boundary layers while simultaneously reducing their thicknesses.

$einf$ is the parameter that causes the strongest increase of vorticity in boundary layers, and causes the biggest reduction of the boundary layer thicknesses. Also, note that the shear layer is weakened at $x/L = 18$ section. However, $kinf$ has the strongest effect on the thickness of boundary layers and the intensity of the shear layer. C_2, C_μ, and $sigma_e$ have similar but weaker effects. This reinforces the first observations done on Figure 6.

To conclude this section, it seems appropriate to establish links between the previous observations and the transport equations for k and ϵ presented section B. An increase of k at the inlet or an increase of C_μ in Eq 4 raise the levels of the turbulence kinetic energy so that the boundary and shear layers are energized.

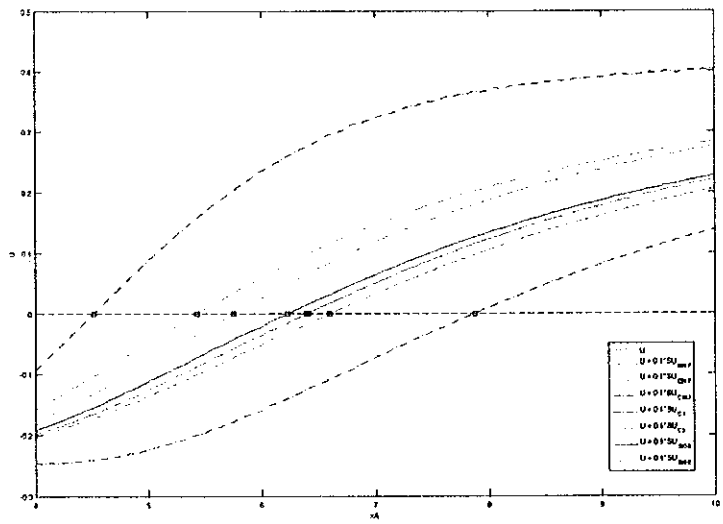

Figure 7. Step: Profiles of u and nearby estimates for the seven parameters

In the same way, any increase in the values of C_2 or σ_ϵ will reduce the rate of dissipation of k. Thus C_μ, C_2,$kinf$ and σ_ϵ affect the flow in the same way.

However, increasing ϵ at the inlet or increasing C_1 raises the rate of dissipation of k. Also, an increase in σ_k reduces the k intensity. Parameters C_1, $einf$ and σ_k have a similar effect. Finally, the two group of influential parameters highlighted through the comments on Figure 7 and Figure 8 are also found from a theoretical analysis. Such an analysis can't be easily followed every time, more particularly when the sensitivities parameters deal with the roughness parameter or the distance from the wall, where the $k-\epsilon$ model is used.

C. Flow past a circular cylinder at Re=10000

Finally URANS results are presented for vortex shedding behind a circular cylinder at a Reynolds number of 10000. Figure 9 illustrates the adaptative mesh obtained after seven cycles of adaptation. As can be seen, the mesh is adapted to the motion of the vortices. Here the mesh exhibits the same alternating patterns as the Karman vortex street because vortex shedding is unimpeded by the presence of any wall. Simulations are performed with the standard $k-\epsilon$ model and the three common variants presented in section D.

The standard $k-\epsilon$ URANS model has a tendency to lock on steady state solutions for valid values of y^+ ($30 \leq y^+ \leq 300$) in the wall functions. This model is characterized by very large values of eddy viscosity in the cylinder's upwind stagnation point region. The production term eq. 6 becomes too high, increases the levels of the TKE which causes local regions of high eddy viscosity. The three variants of the $k-\epsilon$ model examined here all result in lower levels of the eddy viscosity in this area. Hence vortex shedding is not hampered and occurs naturally.

We were interested more particularly in the Strouhal number. Figure 10 shows the grid convergence of the Strouhal number with adaptive mesh refinement for the three variants of $k-\epsilon$ model. All variants seem to converge towards the same value for the Strouhal of about 0.27-0.28. This is very close to the results of B. Mohammadi and O. Pironneau[33] and those of B.A. Younis and V.P. Przulj.[15] However the predicted levels of the Strouhal do not agree well with the experimental measurements results (H. Schlichting[34]).

We now present here a way to work around this problem. The parameter E introduced in section F is

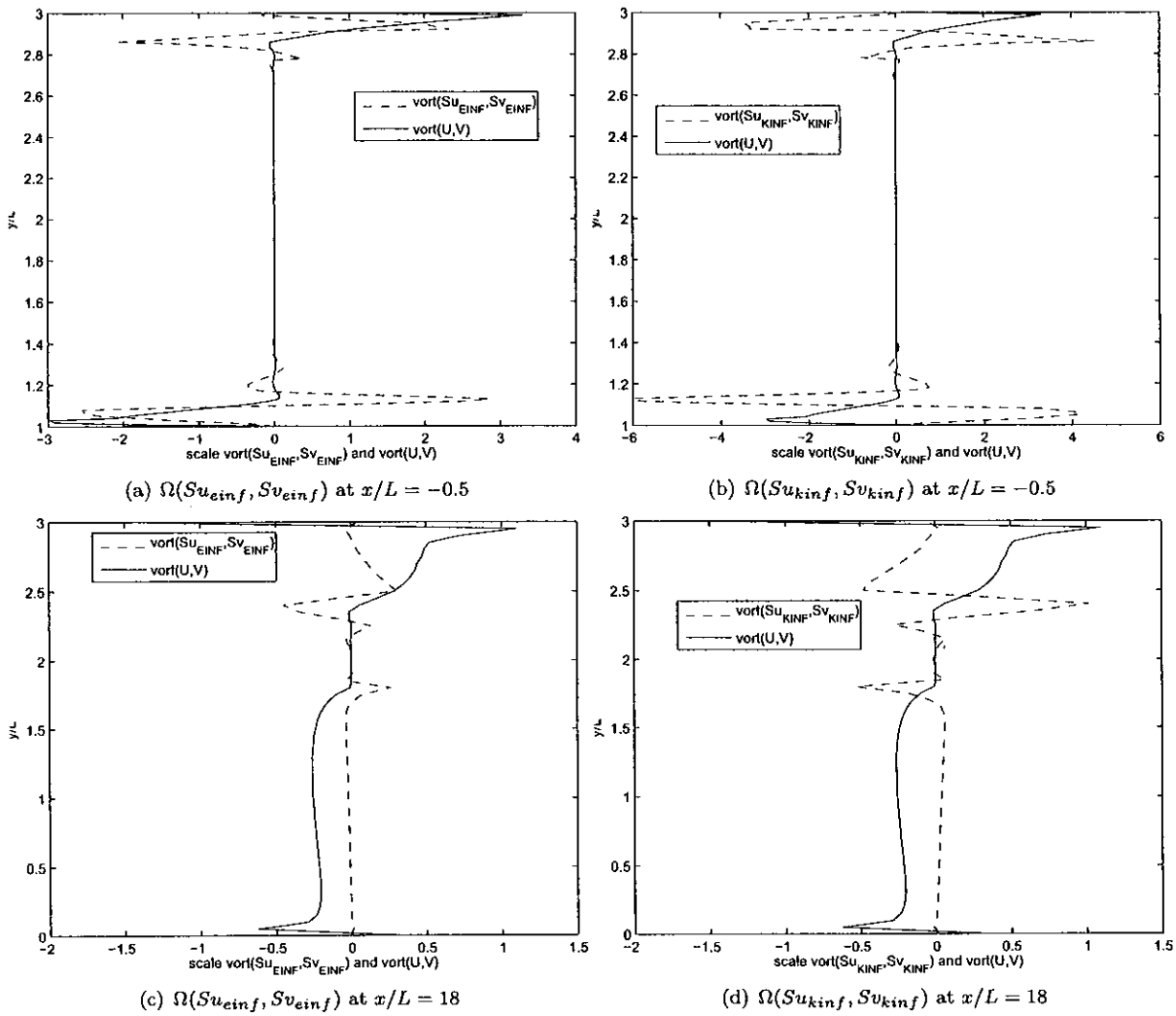

(a) $\Omega(Su_{einf}, Sv_{einf})$ at $x/L = -0.5$

(b) $\Omega(Su_{kinf}, Sv_{kinf})$ at $x/L = -0.5$

(c) $\Omega(Su_{einf}, Sv_{einf})$ at $x/L = 18$

(d) $\Omega(Su_{kinf}, Sv_{kinf})$ at $x/L = 18$

Figure 8. Step: Profiles of the sensitivity vorticity $\Omega(Su, Sv)$ for parameters $kinf$ and $einf$ at time t_f and sections $x/L = -0.5$ and $x/L = 18$

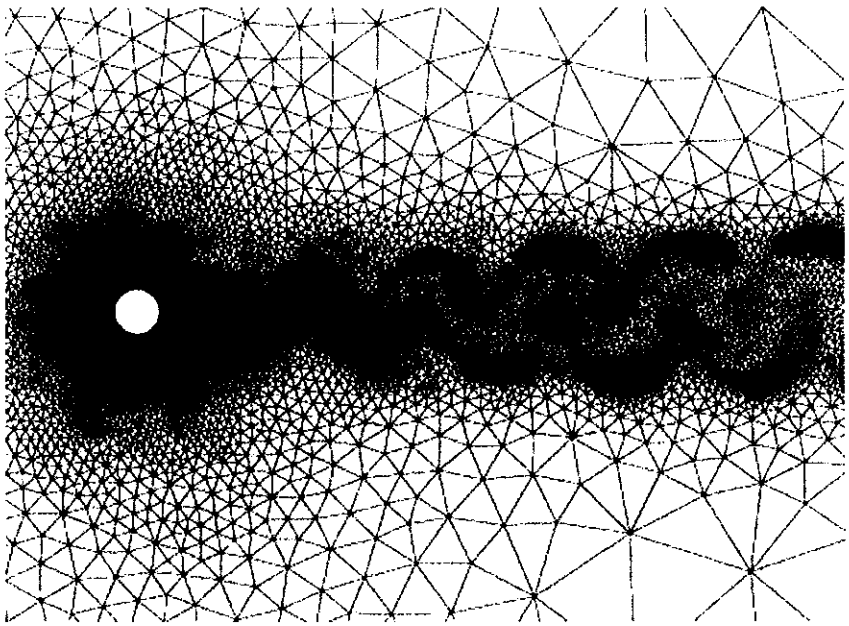

Figure 9. Grid of 90667 nodes for the unsteady simulation with KL

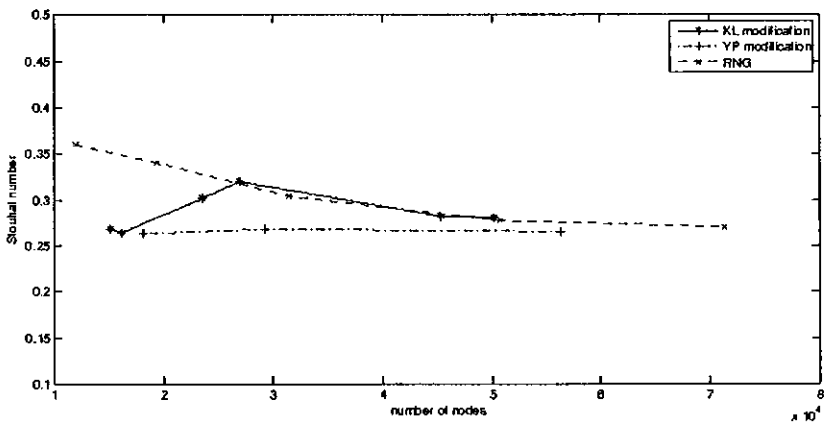

Figure 10. Strouhal number for various meshes obtained with the variants of $k-\epsilon$ model

related to the roughness of the surfaces a value of $E = 9.0$ corresponds to perfectly smooth walls while E is set to $E = 0.3$ characterizes as fully rough surface. Reducing E significantly enhances the prediction of the standard $k - \epsilon$ to captures unsteady phenomena. It seems that the greater the value of E is, the higher the damping of the vortex shedding is. Using this technique, the Strouhal number comes out to be about 0.21 which is very close to the experimental results. The drag and lift coefficients which were completely under-predicted, are also close to the experimental results. Finally, the values of y^+ are greater or equal to 30 which remains in the range of validity of the wall functions.

Three parameters are considered for sensitivity analysis: $U0$, the inflow velocity, $ERUG$, the roughness parameter, and $DPAR$, the wall distance in the wall function. The image on the bottom of Figure 11 shows contours of vorticity for the nominal values of the three parameters, at a given time step in the simulation. The middle image is a contour map of the sensitivity of the nominal vorticity field. The image on top is the estimate of the vorticity field for a perturbation of +20% of the free stream velocity. In other words it is a contour map of the surface described by the Taylor series

$$\Omega(x, y, t; U_0 + \Delta U_o) \approx \Omega(x, y, t; U_0) + \frac{\partial \Omega}{\partial U_0}(x, y, t; U_0) \tag{50}$$

The scales of the top and bottom vorticity contour maps are different because of the 20% difference in the inflow velocity. The middle plot has units of $\frac{1}{m}$ (vorticity over velocity) while the vorticity contours have units $\frac{1}{s}$. The gray vertical line located at $x/D = 5$ serves as a reminder that the range of contour levels have been selected to highlight key features in each case. Downstream of this line, the same contour levels are used to show the magnitude and sign of the three terms in the Taylor series of Eq 50.

The region where vortices are shed ($1 \leq \frac{x}{D} \leq 2$ for the nominal flow becomes smaller (shorter and narrower) and closer to the cylinder for the perturbed flow (top) as one would expect and observe in an experiment. Further more, the sensitivity contour map indicates that the vortices located at $x = 2.5D$ and $x = 4.5D$ on the bottom map will move further downstream in the case of the higher free stream velocity. This is more easily observed by looking the two vortices located at $x = 6$ or $x = 8$ on the bottom image. The vertical black lines have their origin at the center of a vortex and extend upward to serve as a reference to assess the effects of an increase of U_0 on the motion of the vortices in the Von Karman street. As can be seen, the nearby solution clearly shows that its vortices have moved farther downstream than their counterpart in the nominal flow.

Figure 12 shows a 3-D surface view of the nominal vorticity field and its sensitivity with respect to U_0. Notice the relative locations of the local extrema in the vorticity and its sensitivity. Close to the cylinder ($x/D = 2$), the peaks of vorticity is in opposition to that in the sensitivity field. The positive peak in the sensitivity will reduce the depth of the through in the vorticity surface. A little farther downstream ($x/D = 2.4$), a through in the sensitivity field will caused the local minimum in the vorticity filed to more downstream. The two observation confirm that the vortices travel further downstream for the perturbed flow. Finally, the vorticity and sensitivity layers along the surface of the cylinder indicate that increasing U_0 will increase the vorticity in the attached boundary layer on the upwind side of the cylinder, decrease the boundary layer thickness, and move the separation point further to the rear side of the cylinder. All above comments about vorticity and its sensitivity of vorticity show that the sensitivity field predicts a lower Strouhal number for higher values of U_0, a trend consistent with experimental observations for this range of Reynolds numbers.

Figure 13 compares the vorticity of the flow with its sensitivity with respect to $ERUG$, the roughness parameter. Note that the results obtained with the $DPAR$ parameter (the distance from the wall in the wall functions) are quite similar. Here, increasing E (i.e. decreasing the roughness coefficient) results in a damping of the vortex shedding. Indeed, the sensitivity predicts greater and positive values where the vorticity is negative (the top part of the vortex shedding depicted in blue). The outside of the vortex shedding shows greater values, so the width of the vortex street is reduced ; and around the vortices, values with opposite sign are predicted, so that the strength of the vortices is reduced. That goes in the direction of the previous observation : for large values of E, the standard $k - \epsilon$ model damps the vortex shedding.

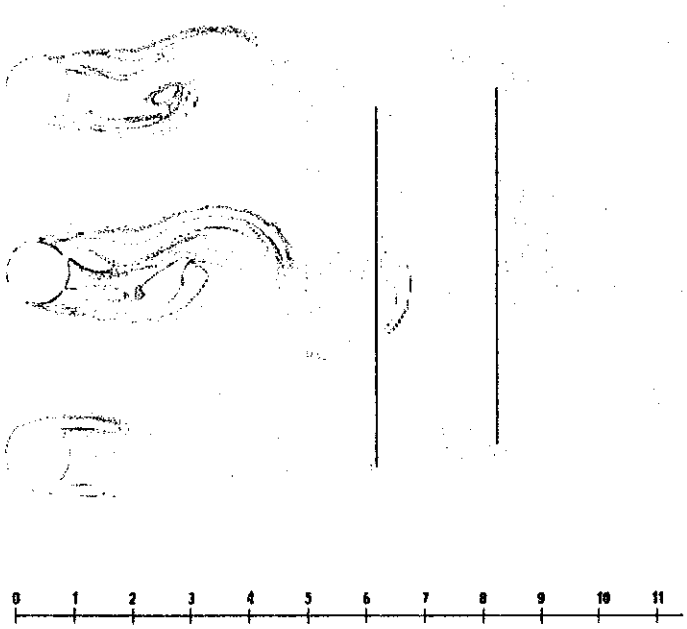

Figure 11. From top to bottom : Vorticity of the nearby solution , Sensitivity of the vorticity with respect to $U0$, vorticity of the flow

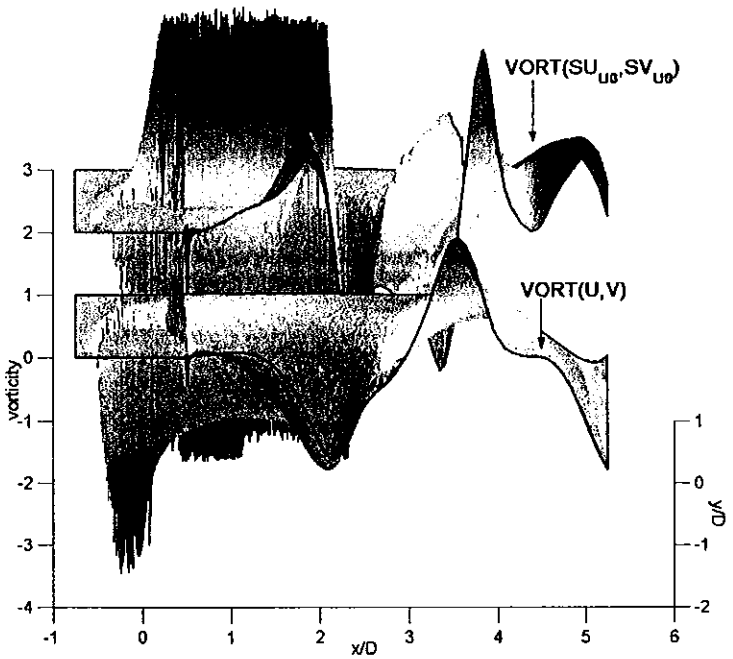

Figure 12. Vorticity Layer and its sensitivity with respect to $U0$

The same holds for $DPAR$ which explains why maintaining y^+ values greater than 30 by solely changing the wall distance proves to be difficult.

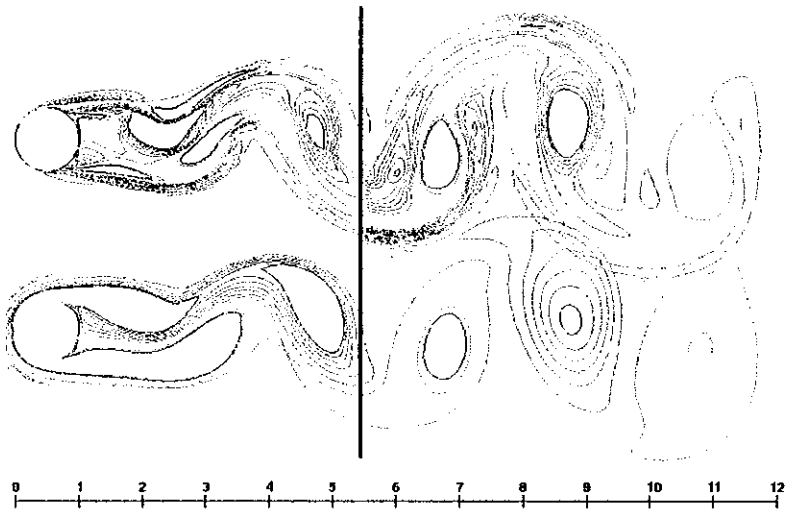

Figure 13. From top to bottom : Sensitivity of the vorticity with respect to $ERUG$, vorticity of the flow

To conclude, Figure 14 shows the drag coefficient computed on the cylinder and its sensitivities with respect to $U0$ and $ERUG$ parameters. As one can guess, an increase of $U0$ raises the drag coefficient. In the opposite, an increase of $ERUG$, so a decrease of the roughness coefficient, reduces the drag coefficient.

VI. Conclusion

A finite Element Formulation for unsteady RANS flow and sensitivity analysis has been presented. The core of the simulation model is the standard $k-\epsilon$ model of turbulence with wall functions. However, three variants improving the vortex shedding predictive capability are tested. Formal differentiation of the URANS equations and their boundary conditions using the implicit function theorem leads to the so-called Eulerian Sensitivities Equation Method (CESEM).The flow and sensitivity equations are advanced in time using an implicit Euler time integrator.

An adaptive remeshing finite element algorithm is used to improve resolution and solution accuracy of important flow features such as shear layers and vortices shed by bluff bodies. The flow and sensitivity solutions are analyzed and error estimates are evaluated to determine where and when the grid must be refined or coarsened and by what factor. The adaptive strategy is applied every few time steps and proves very effective at tracking flow features with uniformly high resolution.

The methodology is verified on the simple case of the decay of grid turbulence. The methodology is the applied to transient turbulent flow over a backward facing step and to vortex shedding behind a circular cylinder. Three variants of the $k-\epsilon$ model aimed at improving its vortex shedding ability were tested. The three variants produce the same value of the Strouhal number when the adaptive grids become fine enough. Predictions are consistent with those of other authors. However, the predicted values agree poorly with measurement. Improved predictions of the Strouhal number are obtained by performing a consistent adjustment of the roughness parameter and wall distance in the wall function so as to maintain it in its range of validity (i.e. $y^+ in [30, 300]$.

Finally, we show several ways of using sensitivity information. Sensitivities are useful to help understand

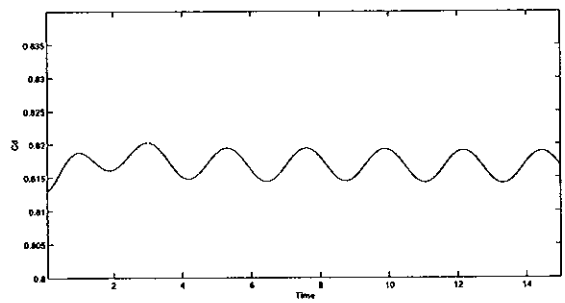

(a) The drag coefficient

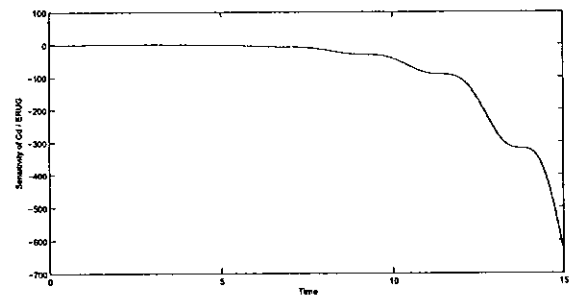

(b) Sensitivity of C_D with respect to $ERUG$

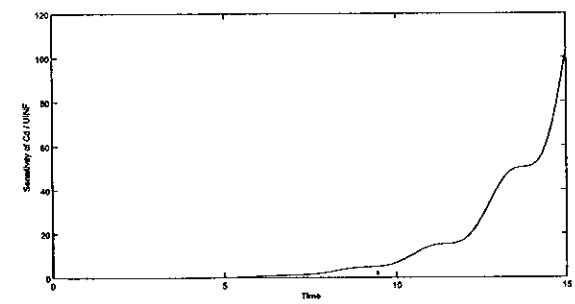

(c) Sensitivity of D_D with respect to $U0$

Figure 14. The C_D and sensitivities with respect to $U0$ and $ERUG$

complex flow phenomena, they provide fast estimates of nearby flows through linear Taylor series in parameter space. This is a powerful tool to answer "what if questions" , ie.e obtain estimates of the flow response without performing a costly simulation at the perturbed values of the parameters. Sensitivity information can be used to rank parameters by order of decreasing importance on the flow response. This proves useful to speed up the solution of an optimal design problem by reducing the number of design parameters. Finally, input data uncertainty can be cascaded through the CFD code to obtain estimates of uncertainty of the flow.

References

[1]R.H Nichols. Development and validation of a two-equations turbulence model with wall functions for compressible flow. In 14^{th} *AIAA Applied Aerodynamics Conference*, New Orleans, LA, 1996. AIAA Paper 96-2385.

[2]N.E. Suhs, R.H. Nichols, and A.G Denny. Unsteady viscous flow computations using two-equations turbulence model with wall functions for compressible flow. In 14^{th} *AIAA Applied Aerodynamics Conference*, New Orleans, LA, 1996. AIAA Paper 96-2430-CP.

[3]T. Schonfeld, O. Colin, and M. Rudgyard. Parallel implementation of $k-\epsilon$ turbulence model with wall functions for unstructured grids. In 27^{th} *AIAA Fluid Dynamics Conference*, New Orleans, LA, 1996. AIAA Paper 96-2061-CP.

[4]B. Mohammadi and G.Puigt. Wall functions in computational fluid mechanics. *Computers and Fluids*, 35:1108–1115, 2006.

[5]F. Hecht and B. Mohammadi. Mesh adaptation by metric control for multi-scale phenomena and turbulence. *AIAA*, 1997. 97-0859.

[6]R. Lohner and J.D. Baum. Adaptative $h-$refinement on 3d unstructured grids for transient problems. *Int. J. Numer. Methods Fluids*, 14:1407–1419, 1992.

[7]R.D. Rausch, J.T. Batina, and H.T.Y. Yang. Spatial adaptation procedures on tetrahedral meshes for unsteady aerodynamics flow calculations. *AIAA*, 30:1243–1251, 1992.

[8]É. Turgeon, D. Pelletier, and J. Borggaard. Application of a sensitivity equation method to the $k-\epsilon$ model of turbulence. In 15^{th} *AIAA Computational Fluid Dynamics Conference*, Anaheim, CA, 2001. AIAA Paper 2001-2534.

[9]É. Turgeon, D. Pelletier, and J. Borggaard. A general continuous sensitivity equation formulation for the $k-\epsilon$ model of turbulence. *International Journal for Numerical Methods in Fluids*, 18(1):29–46, 2004.

[10]P. J. Roache. *Verification and Validation in Computational Science and Engineering*. Hermosa publishers, Albuquerque, New Mexico, 1998.

[11]B.E. Launder and J. Spalding. The numerical computation of turbulent flows. *Computer Methods in Applied Mechanics and Engineering*, pages 269–289, 1974.

[12]F. Ilinca. *Méthodes d'éléments finis adaptatives pour les écoulements turbulents*. PhD thesis, École Polytechnique de Montréal, 1996.

[13]F. Ilinca and D. Pelletier. Positivity preservation and adaptative solution for the $k-\epsilon$ model of turbulence. *AIAA Journal*, 36(1):44–51, 1998.

[14]M. Kato and B.E. Launder. The modeling of turbulent flow around stationary and vibrating square cylinders. In *Proc. 9th Symposium on Turbulent Shear Flows*, Kyoto, Japan, Aug. 1993. 10.4.1–10.4.6.

[15]B.A. Younis and V.P. Przulj. Computation of turbulent vortex shedding. *Computational Mechanics*, 37:408–425, 2006.

[16]V. Yakhot, S.A. Orszag, S. Thangam, T.B. Gatski, and C.G. Speziale. Development of turbulence models for shear flows by a double expansion technique. *Physics of Fluids A*, 4:1510–1520, 1992.

[17]J. P. Chabard. Projet N3S de mécanique des fluides - manuel théorique de la version 3. Technical Report EDF HE-41/91.30B, Électricité de France, 1991.

[18]L. Ignat, D. Pelletier, and F. Ilinca. Adaptive computation of turbulent forced convection. *Numerical Heat Transfer, Part A*, 34:847–871, 1998.

[19]É. Turgeon, D. Pelletier, and J. Borggaard. A general continuous sensitivity equation formulation for complex flows. In 8^{th} *AIAA/NASA/USAF/ISSMO Symposium on Multidisciplinary Analysis and Optimization*, Long Beach, CA, 2000. AIAA Paper 2000-4732.

[20]F. Ilinca, D. Pelletier, and A. Garon. An adaptive finite element method for a two-equation turbulence model in wall-bounded flows. *International Journal for Numerical Methods in Fluids*, 24:101–120, 1997.

[21]O. Schenk and K. Gärtner. Solving unsymmetric sparse systems of linear equations with pardiso. *Journal of Future Generation Computer Systems*, 20(3):475–487, 2004.

[22]O. Schenk and K. Gärtner. On fast factorization pivoting methods for symmetric indefinite systems. *Elec. Trans. Numer. Anal.*, 23:158–179, 2006.

[23]J. Peraire, M. Vahdati, K. Morgan, and O. C. Ziekiewicz. Adaptive remeshing for compressible flow computations. *Journal of Computational Physics*, 72(2):449–466, 1987.

[24]D. Pelletier and F. Ilinca. Adaptive remeshing for the $k-\epsilon$ model of turbulence. *AIAA Journal*, 35(4):640–646, 1997.

[25]O. C. Zienkiewicz and J. Z. Zhu. The superconvergent patch recovery and *a posteriori* error estimates. Part 1: The recovery technique. *International Journal for Numerical Methods in Engineering*, 33:1331–1364, 1992.

[26]O. C. Zienkiewicz and J. Z. Zhu. The superconvergent patch recovery and *a posteriori* error estimates. Part 2: Error estimates and adaptivity. *International Journal for Numerical Methods in Engineering*, 33:1365–1382, 1992.

[27]F. Ilinca, D. Pelletier, and F. Arnoux-Guisse. An adaptive finite element scheme for turbulent free shear flows. *International Journal for CFD*, 8:171–188, 1997.

[28]É. Turgeon. Application d'une méthode d'éléments finis adaptative à des écoulements axisymétriques. Master's thesis, École Polytechnique de Montréal, 1997.

[29]F. Ilinca and D. Pelletier. A unified approach for adaptive solutions of compressible and incompressible flows. In *35th AIAA Aerospace Sciences Meeting and Exhibit*, Reno, Nevada, Jan. 1997. AIAA Paper 97-0330.

[30]J. Borggaard and D. Pelletier. Optimal shape design in forced convection using adaptative finite elements. In *36th AIAA Aerospace Sciences Meeting and Exhibit*, Reno, Nevada, Jan. 1998. AIAA Paper 97-0330.

[31]D. Pelletier, E. Turgeon, S. Etienne, and J. Borggaard. Reliable sensitivity analysis by an adaptative sensitivity equation method. In *3rd AIAA Theoretical fluid mechanics conference*, St-Louis, MO, June 2002. AIAA Paper 2002-2758.

[32]F. Ilinca, D. Pelletier, and L. Ignat. Adaptive finite element solution of compressible turbulent flows. *AIAA*, 12:2187–2194, 1998.

[33]B. Mohammadi and O. Pironneau. Unsteady separated turbulent flows computation with wall-laws and $k - \epsilon$ model. *Computer methods in applied mechanics and engineering*, 148:393–405, 1997.

[34]H. Schlichting. *Boundary layer theory*. McGraw Hill, 1979.